ChemComm

COMMUNICATION

View Article Online
View Journal

Cite this: DOI: 10.1039/d5cc02306h

Received 25th April 2025,
Accepted 16th June 2025

DOI: 10.1039/d5cc02306h

rsc.li/chemcomm

Nuclearity effect on water oxidation: a comparative study of dinuclear and mononuclear iron complexes†

Rong Yan,[abc] Zi-Han Li,[a] Qian-Cheng Luo,[a] Na-Na Sun,*[a] Johnny C. Ho*[bc] and Yan-Zhen Zheng*[a]

A novel dinuclear iron complex $[Fe_2(Pmabt)_2(Pbt)_2][ClO_4]_2{\cdot}2CH_3OH$ (2Fe-4S, Pmbt = 2-(pyridin-2′-yl)benzothiazoline, Pbt = 2-(pyridin-2-yl)benzo[*d*]thiazole) is presented. The electrochemical water oxidation properties manifested that 2Fe-4S exhibits a sevenfold higher TOF value compared to the mononuclear counterpart. Kinetic isotope effects (KIEs) showed the distinct O–O bond formation mechanism of the two complexes, underscoring the significant influence of nuclearity on catalytic behavior in water oxidation processes.

Water oxidation is regarded as the restriction of the water splitting reaction, since it requires overcoming high kinetic and thermodynamic energy, which involves a four-electron transfer.[1] Enhancing the efficiency of oxygen evolution is an essential topic for resolving this problem. The main obstacle is to seek and design efficient catalysts.[2] Molecular catalysts have attracted considerable attention owing to their structural tunability and high atom utilization efficiency.[3,4] Owing to their economical price, abundant reserves, and flexible redox features, transition-metal-based materials are promising over precious metals (ruthenium and iridium) in many ways.[5–9] Iron, located above ruthenium with a similar nature in the periodic table, makes it a quite appealing element for catalysis.[10,11] However, there are relatively few reports on iron-based catalysts compared with other metals.

The catalytic characteristics of molecular catalysts are significantly impacted by the nuclearity.[12–14] According to previously reported cases, binuclear complexes generally possess superior catalytic activities to their analog mono species, given the synergistic catalysis of metal centers.[15,16] Thummel *et al.* synthesized two catalysts for water oxidation: mononuclear complex Fe^{III}(dpa) and a μ-oxo-bridged dimer Fe^{III}(ppq).[17] The TOF value of the latter is ninefold higher than the monomer. Experiments have indicated that the ppq complex goes through a two-electron oxidation, which may result in a $Fe^{III}Fe^{V}{=}O$ intermediate. Wang, Liao, and co-workers developed a bi-copper compound, $[L1Cu_2(\mu\text{-}OH)](BF_4)_3$, along with its mononuclear contrast, $[L2Cu(OH_2)](BF4)_2$, as water oxidation catalysts (WOCs).[18] Comparative studies on catalytic performance revealed that the dinuclear complex exhibited superior activity and stability compared to its mononuclear counterpart. Mechanistic investigations indicated that the short, flexible linker between the Cu centers facilitated intramolecular synergistic interactions, enhancing catalytic efficiency. Additionally, this structural feature helped prevent the accumulation of high-valent intermediates during the catalytic process. Molecular catalytic mechanisms are also relevant to this phenomenon.[19] There are two main types of molecular catalytic mechanisms proposed: (i) water nucleophilic attack (WNA); (ii) the interaction of two metal–oxo units (I2M) or radical coupling.[20,21] The occurrence of the second condition requires proper coordination environments, metal atomic distance, and other factors, which bring metal intermediates with lower valence states, thereby decreasing the reaction energy barrier.

Taking into account the factors mentioned above, we developed and synthesized a novel binuclear iron cluster $[Fe_2(Pmabt)_2(Pbt)_2][ClO_4]_2{\cdot}2CH_3OH$ (**2Fe-4S**, Pmbt = 2-(pyridin-2′-yl)benzothiazoline, Pbt = 2-(pyridin-2-yl)benzo[*d*]thiazole), and a homoligand mononuclear complex $Fe(Pmabt)_2$ (**Fe-2S**, previously reported in ref. 22) was employed for comparison.[22] The two complexes both exhibited water oxidation activity, according to electrochemical studies. Notably, **2Fe-4S** with binuclear iron centers possesses a TOF value of 22.1 s^{-1}, which is a sevenfold enhancement in catalytic efficiency compared to its mononuclear counterpart **Fe-2S** (TOF = 3.3 s^{-1}). Subsequent isotope tests revealed the

[a] *Frontier Institute of Science and Technology, Interdisciplinary Research Center of Frontier Science and Technology, State Key Laboratory of Electrical Insulation and Power Equipment, MOE Key Laboratory for Nonequilibrium Synthesis and Modulation of Condensed Matter, Xi'an Key Laboratory of Electronic Devices and Material Chemistry, and School of Chemistry, Xi'an Jiaotong University, Xi'an, Shaanxi, 710054, P. R. China*

[b] *Department of Materials Science and Engineering, City University of, Hong Kong, 83 Tat Chee Avenue, Kowloon 999077, Hong Kong*

[c] *Shenzhen Research Institute, City University of Hong Kong, Shenzhen 518057, P. R. China*

† Electronic supplementary information (ESI) available. CCDC 2383667 and 2383668. For ESI and crystallographic data in CIF or other electronic format see DOI: https://doi.org/10.1039/d5cc02306h

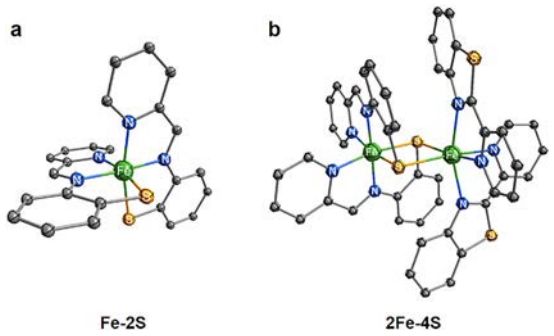

Fig. 1 Displacement ellipsoid plots (at the 50% probability level) of complexes (a) **Fe-2S** and (b) **2Fe-4S** at 150 K. For clarity, all hydrogen atoms and the four triflate counterions have been omitted.

different mechanisms of the two complexes. Moreover, the cyclic mechanisms were also speculated from the experimental results.

High-quality single crystals of complexes **Fe-2S** and **2Fe-4S** were synthesized *via* a straightforward Schiff base condensation using equimolar reactants (Scheme S1, ESI†). Notably, half of the Pmbat ligands were electrochemically oxidized in methanol with sodium perchlorate to yield Pbt ligands. X-ray crystallography confirmed the molecular structures, with full crystal data and refinement parameters provided in the ESI† (Fig. 1 and Tables S1–S6). **Fe-2S** and **2Fe-4S** crystallize in the orthorhombic $Pna2_1$ and triclinic $P\bar{1}$ space groups, respectively. Both complexes are 6-coordinate with a $[FeS_2N_4]$ core. **Fe-2S** is a neutral complex featuring an Fe(II) center bound to two Pmbat ligands *via* deprotonated thiophenate groups. The Fe–S bond lengths are 2.2921(9) and 2.3017(10) Å, while the Fe–N bonds range from 1.914(2) to 1.975(2) Å, with Fe–N(py) being longer (Table S3, ESI†). The Pmbat ligand planes are nearly perpendicular (87.45°). **2Fe-4S** contains two lattice-incorporated methanol molecules, and the dicationic complex $[Fe_2(Pmabt)_2(Pbt)_2]^{2+}$ is charge-balanced by two perchlorate ($[ClO_4]^-$) counterions. Single-crystal X-ray diffraction reveals that the perchlorate salt of the cation complex features an $\{Fe_2S_2N_4\}$ core, where two distinct iron(II) centers are bridged by thiophenate ligands. The Fe1 ion is coordinated by two Pmbat ligands while the Fe2 ion is surrounded by two Pbt ligands. No Fe···Fe interaction is observed, consistent with an Fe···Fe distance of 3.489(2) Å. While Fe1 resembles the **Fe-2S** unit, the Pmbat ligands adopt a crisscross pattern; Fe2 exhibits a distorted octahedral geometry, coordinated by two neutral Pbt ligands, with its coordination environment completed by two sulfur-bridged ligands. The chelating ligand results in Fe2–N bond lengths of 2.202(3) Å (averaged for the two pyridine units), with the five-membered ring donor exhibiting a slightly shorter Fe2–N bond length of 1.956(3) Å. The Fe–S bond lengths range from 2.2957(8) to 2.5118(9) Å. The coordination bond angles reveal significant deviations from ideal octahedral geometry, with the N5–Fe2–N8 angle of 161.26(11)° showing the largest deviation. X-ray powder diffraction measurements of crystalline powder samples showed that the prepared samples were pure phase (Fig. S1 and S2, ESI†). Infrared spectra proved the Fe–S vibration peaks in **2Fe-4S** (Fig. S3, ESI†).

Dc magnetic measurements were performed for complex **2Fe-4S** to determine its ground-state spin configuration (Fig. 2a). Under the external field of 1000 Oe, the $\chi_M T$ product at 300 K is 5.85 $cm^3\ mol^{-1}$ K, which appears to be consistent with the theoretical value of 6 $cm^3\ mol^{-1}$ K for both non-interacting high-spin Fe(II) ions ($g = 2$, $S = 2$). Meanwhile, the linear relation of the $\chi_M T$-T plot in the high temperature regime indicates the contribution of temperature-independent paramagnetism (TIP), and thus the combination of one low-spin and one high-spin state for both Fe(II) centers is more probable. More magnetic analysis and fitting can be found in the ESI.†

A critical consideration is the potential dissociation of the dimeric complex into monomeric species under solution conditions. Electrospray ionization mass spectrometry (ESI-MS) was thus investigated in MeCN solution (Fig. 2b). Electrospray ionization mass spectrometry (ESI-MS) for **Fe-2S**: cal. 482.0317 ($M + e^-$), found m/z^+ = 482.0319. ESI-MS for **2Fe-4S**: cal. 481.0239 (M^{2+}), found m/z^+ = 481.0248. When conducted in MeCN/H_2O, only **2Fe-4S** combined with H_2O $[\mathbf{2Fe\text{-}4S} + H_2O + 2OH]^{2+}$ (m/z^+ = 508.0315, cal: 508.0397) was found (Fig. S4, ESI†).

The electrochemical properties of the two complexes were characterized in MeCN (Fig. 2c and Fig. S5, ESI†). **Fe-2S** displayed a reversible wave at $E_{pc} = -0.58$ V *vs.* Fc/Fc^+ that was attributed to ligand redox, while a quasi-reversible couple at $E_{pa} = 0.41$ V *vs.* Fc/Fc^+ and a reversible redox peak at $E_{pa} = 1.05$ V *vs.* Fc/Fc^+ were observed. The CV of **2Fe-4S** exhibited similar behaviors. A reduction process was observed at −0.57 V *vs.* Fc/Fc^+ due to the slight difference in the ligands. A second quasi-reversible couple is observed at 0.36 V *vs.* Fc/Fc^+, and an extra peak appears at 0.52 V *vs.* Fc/Fc^+, which is the oxidation of the second iron atom. The same reversible wave appears as the **Fe-2S** at $E_{pa} = 1.05$ V *vs.* Fc/Fc^+. The peaks around 0.4 V and 1.0 V *vs.* Fc/Fc^+ are assigned to $Fe^{III/II}$ and $Fe^{IV/III}$ couples.[23,24] Both large catalytic currents emerge when adding H_2O as a substrate, indicating the catalytic effect on water oxidation of the two complexes (Fig. S6, ESI†). When the

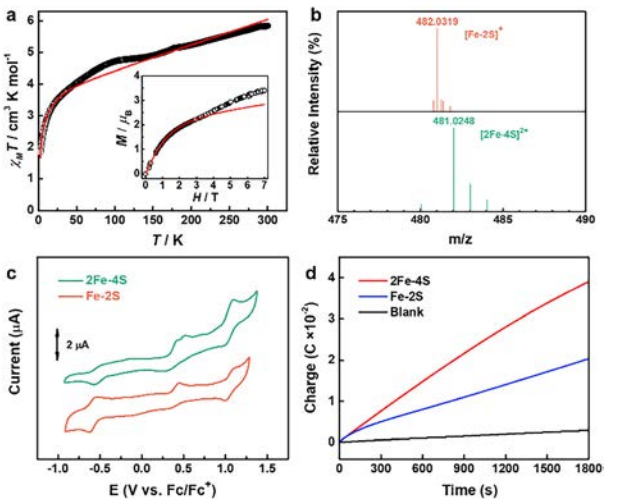

Fig. 2 (a) Temperature dependence of the $\chi_M T$ product for **2Fe-4S** under a 5000 Oe dc field (inset: the magnetization data of **2Fe-4S** at 2 K). The red solid lines represent the best fit through PHI software.[33] (b) ESI-MS of **Fe-2S** and **2Fe-4S**. (c) CVs of 0.2 mM **Fe-2S** and **2Fe-4S** in MeCN with Bu_4NPF_6 (0.1 M), 10 mV s^{-1}. (d) Q–t curves at 1.42 V *vs.* Fc/Fc^+, with 0.2 mM of **2Fe-4S**, **Fe-2S**, and without the complex.

same voltage is applied to the onset potential, the catalytic current of **2Fe-4S** was about 1.5 times larger than that of **Fe-2S**, indicating the superior activity of the diiron complex.

Controlled-potential electrolysis (CPE) experiments were performed using a 1 × 3 cm^2 ITO working electrode, which further validated the quantities of generated oxygen (Fig. 2d and Fig. S7, ESI†). At applied potentials of 1.19 V and 1.38 V *vs.* Fc/Fc^+, **Fe-2S** and **2Fe-4S** exhibited notable and stable charge accumulation compared to a negligible response with no complexes added. The pH value after CPE decreased from 6.6 to 6.2 for **Fe-2S** and 6.5 to 6.2 for **2Fe-4S**. By adjusting the pH to the initial state, the catalytic current for both catalysts could be restored partly (Fig. S8, ESI†). The generated oxygen was also measured by gas chromatography (GC) during CPE (Fig. S9 and S10, ESI†). O_2 bubbles generated on the surface of the working electrode could be observed (Fig. S11, ESI†). The concentration of O_2 in the headspace of the tube increased to 2.2 μL for **2Fe-4S** with Faraday efficiency (FE) of 97.6% and to 1.1 μL for **Fe-2S** with FE of 94.8%, which is negligible for the blank experiment without catalysts, also indicating the superior catalytic water oxidation activity of **2Fe-4S** to **Fe-2S**.

For molecular catalysts, it is vital to determine the true active ingredient, which determines whether the reaction is homogeneous. Therefore, we carried out a series of stability tests. CVs before and after CPE were conducted, and negligible decay of catalytic currents on both complexes was observed (Fig. S12, ESI†). Scanning electron microscopy (SEM) and energy dispersive X-ray spectroscopy (EDX) analysis revealed morphological and compositional changes in the ITO electrode following CPE operation. SEM analysis reveals that the surface morphology of the ITO electrode remains consistent before and after the reaction, with no precipitation of iron oxide observed during electrolysis (Fig. S13, ESI†). Additionally, EDX spectra indicate negligible deposition of Fe elements on the electrode surface after CPE (Fig. S14, ESI†). HR-MS after CPE for both complexes was investigated and kept consistent with initial structures (Fig. S15, ESI†). These findings collectively demonstrate that **Fe-2S** and **2Fe-4S** remain homogeneous throughout the catalytic process.

Constant limiting currents were observed, with **Fe-2S** showing the highest catalytic current at 10.1 mM H_2O, and **2Fe-4S** maximum peaking at 5.6 mM. These concentrations were selected for all further experiments, indicating that substrate levels were sufficient to reach the purely kinetic condition (Fig. S16 and S17, ESI†). Catalyst concentration studies revealed a linear relationship between i_{cat} and [cat] in the 0.2–1.5 mM range (Fig. S18–S21, ESI†), suggesting a pseudo-first-order rate law: $d[O_2]/dt = k_{cat}[cat]$. Peak currents also scaled linearly with scan rate, consistent with diffusion-controlled processes (Fig. 3a and Fig. S22, ESI†). Notably, **2Fe-4S** exhibited a turnover frequency (TOF) of 22.1 s^{-1}, nearly seven times higher than **Fe-2S** (3.3 s^{-1}) (Fig. 3b and Fig. S23 (ESI†); TOF calculations in Tables S7 and S8, ESI†). The TONs were 5940 and 39 780 for **Fe-2S** and **2Fe-4S** within the CPE period, respectively. This highlights the superior catalytic performance of the binuclear complex, likely due to a nuclearity-driven mechanism difference.

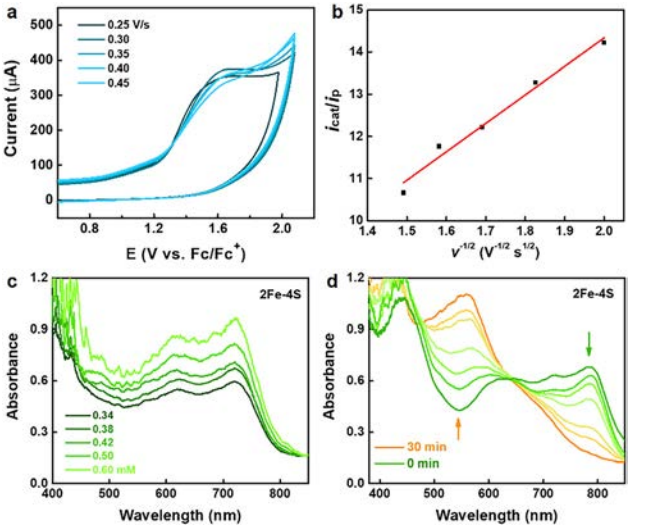

Fig. 3 (a) CVs of **2Fe-4S** (0.2 mM) in MeCN/H_2O (8 : 2) with 0.1 M Bu_4NPF_6, scan rates of 0.25–0.40 V s^{-1}. (b) Plot of ratio for i_{cat}/i_p as a function of $\nu^{-1/2}$ for **2Fe-4S**. (c) UV-Vis of various concentrations of **2Fe-4S** in MeCN. (d) *In situ* UV-Vis spectra change during the reaction for **2Fe-4S**.

We also studied the electronic behavior of the **Fe-2S** and **2Fe-4S** systems by UV-Vis spectroscopy in MeCN. **Fe-2S** exhibits two intense bands in the visible region, 420 and 790 nm, assigned to the $p\pi \rightarrow d\pi^*_{iron}$ charge transfer band and d–d transition (Fig. S24a, ESI†).[25,26] **2Fe-4S** displays bands at 616 and 720 nm, both corresponding to d–d transitions (Fig. S24c, ESI†).[27] The absorbance intensities are linearly dependent on the concentration of **2Fe-4S** within the range from 0.34 to 0.60 mM (Fig. 3c and Fig. S24d, ESI†), suggesting that the binuclear catalyst remains most likely intact in solution. The CPE for the two complexes leads to the slow isosbestic conversion of the green solution to yellow species with a broad band at 550 nm, which is consistent with the Fe^{II} d–d transitions (Fig. 3d and Fig. S24b, ESI†).

Further investigations were conducted on the H_2O/D_2O kinetic isotope effects ($KIE_{H/D}$) to corroborate the proposed reaction pathways.[28] $KIE_{H/D}$ was determined to be approximately 22.5 according to the reported equation for **Fe-2S** (Fig. S25a, ESI†).[29] The detection of a primary kinetic isotope effect using deuterium substitution implicates OH bond cleavage as a vital step in the formation of O–O bonds, validating the WNA mechanism for the **Fe-2S** system. Under homogeneous catalytic conditions, the *I*–*t* curves of **2Fe-4S** in H_2O and D_2O electrolytes were compared, revealing no significant H_2O/D_2O kinetic isotope effects ($KIE_{H/D} \approx 1.83 < 2$) (Fig. S25b, ESI†). This KIE value demonstrates that O–H bond breaking is not rate-limiting in the **2Fe-4S**-mediated water oxidation cycle, aligning with the characteristics of the I2M mechanism.

Based on the above results and previous research, the possible catalytic cycle of **2Fe-4S** could be deduced as follows (Fig. 4): Fe_2^{II} is first oxidized into Fe_2^{III} and coupled with water to form H_2O–Fe^{III}–Fe^{III}–OH_2. It then eliminates $2H^+/2e^-$ to turn into HO–Fe^{IV}–Fe^{IV}–OH and recurs the previous step to remove another $2H^+/2e^-$ to form the transition state, along with the formation of

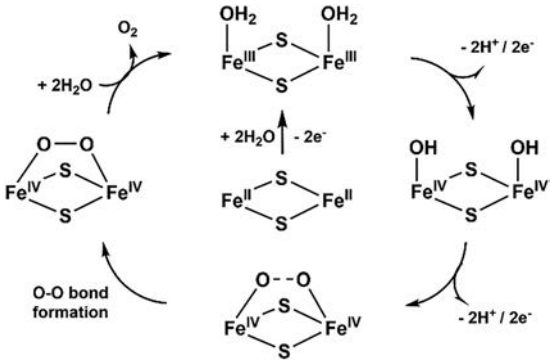

Fig. 4 Possible mechanism for water oxidation of **2Fe-4S**.

an O–O bond. Oxygen is produced after the I2M process creates the Fe^{IV}–O–O–Fe^{IV},[30–32] finishing the catalytic cycle. During the whole process, the highest valence state of the Fe ion is +4, which is noteworthy because it shows that the intramolecular coupling mechanism effectively avoids the generation of high valence intermediates, which is beneficial to the catalytic reaction. Additionally, it has been demonstrated that the binuclear synergistic effects are advantageous to the catalytic activity.

In summary, a dinuclear iron complex, **2Fe-4S**, was successfully synthesized by modifying the iron salt source to introduce perchlorate ions, yielding a dimeric structure closely resembling that of the mononuclear analogue **Fe-2S**. Both complexes were prepared through aldimine condensation, accompanied by *in situ* oxidation of the ligands. The redox behaviors of the two compounds are quite similar, and water oxidation tests displayed that the TOF value of **2Fe-4S** is seven times higher than that of **Fe-2S**. KIEs showed that the two catalysts undergo different catalytic pathways, in which **2Fe-4S** was likely to generate a synergistic impact through the coupling of two adjacent metals within the molecule, avoiding the formation of Fe^{V}═O intermediates, thereby decreasing the reaction energy barrier and enhancing the activity of water oxidation. Future work will aim to elucidate the structures of key catalytic intermediates, explore the in-depth mechanism of the reaction process, and develop a series of analogues to enable systematic performance comparison and structure–activity correlation.

Conflicts of interest

There are no conflicts to declare.

Data availability

All relevant data are within the manuscript and its ESI.†

Notes and references

1 T. E. Jones, D. Teschner and S. Piccinin, *Chem. Rev.*, 2024, **124**, 9136–9223.
2 C. Hu, Y. Hu, B. Zhang, H. Zhang, X. Bao, J. Zhang and P. Yuan, *Electrochem. Energy Rev.*, 2024, **7**, 19.
3 M. Kondo, H. Tatewaki and S. Masaoka, *Chem. Soc. Rev.*, 2021, **50**, 6790–6831.
4 A. Ghaderian, S. Kazim, M. Khaja Nazeeruddin and S. Ahmad, *Coord. Chem. Rev.*, 2022, **450**, 214256.
5 A. G. Nash, C. J. Breyer, B. D. Vincenzini, G. I. Elliott, J. Niklas, O. G. Poluektov, A. L. Rheingold, D. K. Smith, D. G. Musaev and D. B. Grotjahn, *Angew. Chem., Int. Ed.*, 2021, **60**, 1540–1545.
6 B. Van Dijk, G. M. Rodriguez, L. Wu, J. P. Hofmann, A. Macchioni and D. G. H. Hetterscheid, *ACS Catal.*, 2020, **10**, 4398–4410.
7 Q.-F. Chen, Z.-Y. Cheng, R.-Z. Liao and M.-T. Zhang, *J. Am. Chem. Soc.*, 2021, **143**, 19761–19768.
8 J. Hessels, E. Masferrer-Rius, F. Yu, R. J. Detz, R. J. M. Klein Gebbink and J. N. H. Reek, *ChemSusChem*, 2020, **13**, 6629–6634.
9 M. Bera, S. Kaur, K. Keshari, D. Moonshiram and S. Paria, *Inorg. Chem.*, 2022, **61**, 21035–21046.
10 J. D. Blakemore, R. H. Crabtree and G. W. Brudvig, *Chem. Rev.*, 2015, **115**, 12974–13005.
11 Q.-F. Chen, Y.-H. Guo, Y.-H. Yu and M.-T. Zhang, *Coord. Chem. Rev.*, 2021, **448**, 214164.
12 I. G. Powers, J. M. Andjaba, X. Luo, J. Mei and C. Uyeda, *J. Am. Chem. Soc.*, 2018, **140**, 4110–4118.
13 L. Li, M. V. Metz, H. Li, M.-C. Chen, T. J. Marks, L. Liable-Sands and A. L. Rheingold, *J. Am. Chem. Soc.*, 2002, **124**, 12725–12741.
14 H. Li and T. J. Marks, *Proc. Natl. Acad. Sci. U. S. A.*, 2006, **103**, 15295–15302.
15 Q. Huang, J. Chen, P. Luan, C. Ding and C. Li, *Chem. Sci.*, 2022, **13**, 8797–8803.
16 W. Sinha, A. Mahammed, N. Fridman and Z. Gross, *ACS Catal.*, 2020, **10**, 3764–3772.
17 L. D. Wickramasinghe, R. Zhou, R. Zong, P. Vo, K. J. Gagnon and R. P. Thummel, *J. Am. Chem. Soc.*, 2015, **137**, 13260–13263.
18 X. Zhang, Y.-Y. Li, J. Jiang, R. Zhang, R.-Z. Liao and M. Wang, *Inorg. Chem.*, 2020, **59**, 5424–5432.
19 M. J. Craig, G. Coulter, E. Dolan, J. Soriano-López, E. Mates-Torres, W. Schmitt and M. García-Melchor, *Nat. Commun.*, 2019, **10**, 4993.
20 M. Sutradhar, A. J. L. Pombeiro and J. A. L. Da Silva, *Coord. Chem. Rev.*, 2021, **439**, 213911.
21 S. Romain, L. Vigara and A. Llobet, *Acc. Chem. Res.*, 2009, **42**, 1944–1953.
22 Z.-L. Xie, D. L. Pennington, D. G. Boucher, J. Lo and M. J. Rose, *Inorg. Chem.*, 2018, **57**, 10028–10039.
23 V. K. K. Praneeth, M. Kondo, M. Okamura, T. Akai, H. Izu and S. Masaoka, *Chem. Sci.*, 2019, **10**, 4628–4639.
24 S. M. Al-Zuraiji, T. Benkó, L. Illés, M. Németh, K. Frey, A. Sulyok and J. S. Pap, *J. Catal.*, 2020, **381**, 615–625.
25 G. Chen, W. W. Y. Lam, P. Lo, W. Man, L. Chen, K. Lau and T. Lau, *Chem. Eur. J.*, 2018, **24**, 18735–18742.
26 E. Lambert, B. Chabut, S. Chardon-Noblat, A. Deronzier, G. Chottard, A. Bousseksou, J.-P. Tuchagues, J. Laugier, M. Bardet and J.-M. Latour, *J. Am. Chem. Soc.*, 1997, **119**, 9424–9437.
27 J. Moll, C. Förster, A. König, L. M. Carrella, M. Wagner, M. Panthöfer, A. Möller, E. Rentschler and K. Heinze, *Inorg. Chem.*, 2022, **61**, 1659–1671.
28 Z. Chen, J. J. Concepcion, X. Hu, W. Yang, P. G. Hoertz and T. J. Meyer, *Proc. Natl. Acad. Sci. U. S. A.*, 2010, **107**, 7225–7229.
29 D. Wang and J. T. Groves, *Proc. Natl. Acad. Sci. U. S. A.*, 2013, **110**, 15579–15584.
30 A. M. Geer, C. Musgrave Iii, C. Webber, R. J. Nielsen, B. A. McKeown, C. Liu, P. P. M. Schleker, P. Jakes, X. Jia, D. A. Dickie, J. Granwehr, S. Zhang, C. W. Machan, W. A. Goddard and T. B. Gunnoe, *ACS Catal.*, 2021, **11**, 7223–7240.
31 M. Okamura, M. Kondo, R. Kuga, Y. Kurashige, T. Yanai, S. Hayami, V. K. K. Praneeth, M. Yoshida, K. Yoneda, S. Kawata and S. Masaoka, *Nature*, 2016, **530**, 465–468.
32 H.-T. Zhang, X.-J. Su, F. Xie, R.-Z. Liao and M.-T. Zhang, *Angew. Chem., Int. Ed.*, 2021, **60**, 12467–12474.
33 N. F. Chilton, R. P. Anderson, L. D. Turner, A. Soncini and K. S. Murray, *J. Comput. Chem.*, 2013, **34**, 1164–1175.

